The key role of the western boundary in linking the AMOC strength to the north-south pressure gradient.

Willem P. Sijp*, Jonathan M. Gregory **, Remi Tailleux *** and Paul Spence*.

Climate Change Research Centre (CCRC), University of New South Wales, Sydney, New South Wales, Australia

December 8, 2011

Journal of Physical Oceanography

Accepted December 6, 2011

* *Corresponding author address*: Willem P. Sijp, Climate Change Research Centre (CCRC), University of New South Wales, Sydney, NSW 2052, Australia. E-mail: w.sijp@unsw.edu.au

** Department of Meteorology of the University of Reading and Met Office Hadley Centre.

*** Department of Meteorology of the University of Reading.

Abstract

A key idea in the study of the Atlantic meridional overturning circulation (AMOC) is that its strength is proportional to the meridional density gradient, or more precisely, to the strength of the meridional pressure gradient. A physical basis that would tell us how to estimate the relevant meridional pressure gradient locally from the density distribution in numerical ocean models to test such an idea, has been lacking however. Recently, studies of ocean energetics have suggested that the AMOC is driven by the release of available potential energy (APE) into kinetic energy (KE), and that such a conversion takes place primarily in the deep western boundary currents. In this paper, we develop an analytical description linking the western boundary current circulation below the interface separating the North Atlantic Deep Water (NADW) and Antarctic Intermediate Water (AAIW) to the shape of this interface. The simple analytical model also shows how available potential energy is converted into kinetic energy at each location, and that the strength of the transport within the western boundary current is proportional to the local meridional pressure gradient at low latitudes. The present results suggest, therefore, that the conversion rate of potential energy may provide the necessary physical basis for linking the strength of the AMOC to the meridional pressure gradient, and that this could be achieved by a detailed study of the APE to KE conversion in the western boundary current.

1. Introduction

The Atlantic Meridional Overturning Circulation (AMOC) transports heat poleward, and so has a significant role in high-latitude climate (e.g. Manabe and Stouffer 1988, 1999; Vellinga and Wood 2002). It is increasingly recognised that understanding its variability and propensity to change requires understanding the links between the sinking rate, the surface density distribution and the thermal structure of the oceans. (Gnanadesikan et al. 2007). Of particular interest is the relationship between some measure of the Atlantic meridional density gradient and the AMOC strength, which many studies have assumed to be linear (e.g. Robinson and Stommel 1959; Rahmstorf 1996). This generally involves the use of an unconstrained scaling constant, or "fudge factor". A central objective of this paper is to seek a more physical basis for this constant.

Classical scaling (Robinson and Stommel 1959; Robinson 1960) uses the geostrophic thermal wind equation to give a relationship $V = \frac{g}{f}\frac{\Delta_x \rho}{\rho_0}\frac{H}{L_x}$, where V is a scale for the meridional velocity, f the Coriolis parameter, $\Delta_x \rho$ the zonal density gradient across the basin, L_x a zonal length scale, H a characteristic depth of the meridional velocities in the upper flow and ρ_0 an average ocean density. This approach relates to the upper flow of the AMOC, with V located there. To arrive at a relationship involving $\Delta_y \rho$, Robinson (1960) links $\Delta_y \rho$ to $\Delta_x \rho$ via an ad-hoc assumed proportionality $V \propto U$. Marotzke (1997) lists plausible assumptions to justify this type of link. Wright and Stocker (1991) introduce an ad-hoc parameterisation of the zonal pressure gradients in terms of the meridional pressure gradient in their two dimensional latitude-depth ocean model, while Wright et al. (1995) solve this issue with zonally averaged models by using a dynamical link between vorticity dissipation in the western boundary layer and the meridional overturning circulation.

Classical scaling $M \propto gH^2\Delta_y\rho$ for the overturning strength $M = HV$ yields a linear scaling in $\Delta_y\rho$ when H remains constant. This is found in simulations with ocean general circulation models (OGCMs) where surface fresh water fluxes change by Rahmstorf (1996) and others (e.g. Hughes and Weaver 1994; Thorpe et al. 2001; Levermann and Griesel 2004; Griesel and Morales-Maqueda 2006; Dijkstra 2008). In theories where the return flow is linked to H by diffusion (Bryan 1987) or by SO eddies (Gnanadesikan 1999), a different scaling is found. In particular, Gnanadesikan (1999) keeps $\Delta_y\rho$ fixed, and a cubic equation in H is found by closing the mass balance. Levermann and Fuerst (2010) conduct an extensive range of OGCM simulations, and find that both H and $\Delta_y\rho$ are free to change, depending on the nature of the applied perturbation. Park and Whitehead (1999) show a quadratic scaling between flow and an idealised density difference in laboratory experiments, extending the evidence for scaling laws beyond the realm of numerical models.

Instead of using geostrophy, Gnanadesikan (1999) based his scaling law on the balance $A_H\frac{\partial^2 v}{\partial^2 x} = \frac{1}{\rho}\frac{\partial p}{\partial y}$ in the (upper) western boundary current (WBC). Note that he chooses $\Delta_y\rho$ to remain fixed for his purposes, and leaves H free to evolve. Here, A_H is the horizontal viscosity, gradients in pressure p arise from sea surface height gradients and ρ is density. This procedure avoids the need to link the zonal and meridional pressure gradients, but a free constant representing the effects of geometry and boundary layer structure now enters the scaling. This factor is chosen to obtain the overturning rate of his numerical ocean model.

Schewe and Levermann (2010) use essentially this scaling to arrive at a linear scaling for the relationship between the meridional density gradient at 1100m depth and the North Atlantic Deep Water (NADW) outflow rate. This viscous western boundary current approach appears distinct from the approach based on geostrophy, and the relationship between the various approaches is unclear.

Appropriate to their stated purposes, scaling studies make general statements about power-laws between diagnostics, and so tend to involve an undetermined scaling constant. This "fudge factor" can be chosen relatively arbitrarily to arrive at the desired overturning rate. In the present study, we wish to obtain its value explicitly from density properties that appear in the local momentum balance in the numerical model. Here, the meridional slope of the Antarctic Intermediate Water (AAIW)-NADW interface at the western Atlantic boundary turns out to be key.

In addition to examining the nature of the scaling constant, further insight into the relationship between the meridional (frictional) argument (e.g. Gnanadesikan 1999; Schewe and Levermann 2010) and the geostrophic argument (e.g. Robinson 1960; Marotzke 1997) is given via the shape of the interface between the NADW and AAIW water masses. Our approach is related to the scaling study of Schewe and Levermann (2010), and we build on their approach by relating the meridional pressure gradient at the NADW depth range to the overlying interfacial surface h between NADW and AAIW locally. Furthermore, we find a formula for the overturning rate in terms of basic model parameters (e.g. viscosity), the depth of the flow and the meridional slope of the AAIW-NADW interfacial isopycnal in the western boundary (WB) and the meridional density gradient.

2. The Model and Experimental Design

We use Version 2.8 of the intermediate complexity global climate model described in detail in Weaver et al. (2001). This consists of an ocean general circulation model (GFDL MOM Version 2.2 Pacanowski 1995) coupled to a simplified one-layer energy-moisture balance model for the atmosphere and a dynamic-thermodynamic sea-ice model of global domain and horizontal resolution 1.8° longitude by 1.8° latitude (note that the zonal resolution is greater than in the standard configuration). The number of vertical levels has been increased from the standard 19 levels to 51 levels, with enhanced resolution in the upper 200m. This is to better resolve isopycnal slopes, a quantity discussed in this paper. We implemented the turbulent kinetic energy scheme of Blanke and Delecluse (1993) based on Gaspar et al. (1990) to achieve vertical mixing due to wind and vertical velocity shear. A rigid lid approximation is used. The bathymetry consists of a flat bottom at 5500m deep with a 2500m deep sill at “Drake Passage”, and incorporates two idealised basins and a circumpolar “Southern Ocean”, as shown in Figure 3. Heat and moisture transport takes place via advection and Fickian diffusion. We employ a latitudinally varying atmospheric moisture diffusivity, as described in Saenko and Weaver (2003). Air-sea heat and freshwater fluxes evolve freely in the model, yet a non-interactive wind field is employed. The wind forcing consists of zonal averages of the NCEP/NCAR reanalysis fields (Kalnay et al. 1996), averaged over the period 1958-1997 to form a seasonal cycle from the monthly fields. Oceanic vertical mixing in the control case is represented using a diffusivity that increases with depth, taking a value of 0.1 cm^2/s at the surface and increasing to 0.4 cm^2/s at the bottom. The effect of sub-grid scale ocean eddies on tracer transport is modelled by the parameterizations of Gent and McWilliams (1990), using identical thickness and isopycnal diffusivity of 500 m^2/s. Neutral physics in regions of steeply sloping isopycnals is handled by quadratic tapering as described by Gerdes et al. (1991), using a maximum slope of one in a hundred. We will refer to this model as “the numerical model” or the “General Circulation Model” (GCM) to distinguish it from our analytical model. The model has been integrated for 5500 years.

3. Results

GCM circulation and water masses.

Figure 1 shows the Atlantic meridional streamfunction. A northern sinking cell overlies an Antarctic Bottom Water (AABW) cell of about 3 Sv, separated around 2500m depth. The NADW outflow of 10.5 Sv and deep sinking of 18 Sv is similar to that found for instance in the realistic bathymetry configuration of the UVic model discussed in Sijp and England (2004). Most of the NADW recirculation occurs at high northern latitudes (north of 45 $^\circ$N), and equatorial upwelling is limited. The lower limb of the AMOC consists of a narrow deep WB current at low latitudes, as shown for 2160m depth in Fig. 2. No significant horizontal recirculation occurs inside the basin interior, and flow is confined to the WB.

The NADW and AAIW water masses in the Atlantic are moving in opposite directions (see

Fig. 1), and it is of interest to examine an interfacial isopycnal h between the two, shown in Figure 3. Along the western boundary, h exhibits shoaling north of the equator, and deepening to the south. The low-latitude interior of h is relatively horizontal, while h deepens and then shoals at higher latitude as one moves to the northern boundary. These features are absent in the Pacific basin, where deep sinking is absent, and therefore are likely to be a signature of deep water formation in the Atlantic. The meridional slope in the interior of h away from the Equator is associated with significant zonal flow fed by deep sinking along the northern boundary and the Antarctic Circumpolar Current (ACC) at the southern boundary, as can be seen for the northern hemisphere in Figure 2. Here, we will limit discussion to the low latitudes, where the slope of h in the interior is relatively weak, and deep flow is generally meridional along the WB.

Conceptual model and relationship between the interface depth and the circulation

Figure 4 shows a schematic side-on view of the AMOC lower limb (here the southward flow of NADW) and the overlying AAIW in the Atlantic at low latitudes, where the fluid is divided into two homogenous layers. The idealised flow is imagined to take place in the central (narrowest) basin shown in Fig. 3, where the formation of NADW is located, and this basin is referred to as the Atlantic. We take a two dimensional scalar h such that $z = h(x, y)$ coincides with an isopycnal on the water mass interface, also denoted by h. Note that we choose z to increase upwards with $z = 0$ at the surface. In the ocean interior away from the WB, the surface h has negligible zonal slope $\frac{\partial h}{\partial x}$ and meridional slope $\frac{\partial h}{\partial y}$ (dashed line), whereas h has a positive meridional slope $\frac{\partial h}{\partial y}$ at the WB (solid line). Note that this implies that the surface has a finite $\frac{\partial h}{\partial x}$ there.

We will see that $\frac{\partial h}{\partial y}$ has an approximately constant value s_y along the western boundary, where we define $s_y \equiv \frac{\Delta h}{\Delta y}\Big|_{WB}$ with the change Δ taken between 10 °S and 10 °N. For convenience, we take $x = 0$ at the WB, so that $h|_{WB} = h(0, y)$. The general flatness of h away from the WB at low latitudes in the Atlantic (Fig. 3) means that h remains very close to its average value $\bar{h}$ (at low Atlantic latitudes) almost everywhere except in the WBC. We see from Fig. 3 that $h(0, 0) \approx \bar{h}$ (that is h attains its low latitude (e.g. between 20 °S and 20 °N) basin-average value $\bar{h} \approx 1250m$ at the equator). Namely, $h(0, y)$ is shallower than this average north of the equator and deeper to the south (this will be more clearly visible in Fig. 7 and Fig. 8). This will be a feature of our analytical solutions below, and is presently indicated by the intersection of the dashed and solid lines at the Equator in the diagram (Fig. 4). As a result, we can determine $\bar{h}$ from the GCM either via $\bar{h} = h(0, 0)$, or as the low latitude basin average of h (e.g. between 10 °S and 10 °N).

We assume that the interface h resides inside a vertical range of no motion and vanishing pressure gradients. It separates the northward-flowing AAIW and southward-flowing NADW layers. On the interface, ocean surface pressure gradients are balanced by baroclinic gradients (assumption 1 below). However, $h(0, y) > \bar{h}$ (i.e. is more shallow than $\bar{h}$) for $y > 0$, and vice versa for $y < 0$. As a result, below the interface, horizontal pressure gradients arise, where a taller (where the top is at h) than average column of water at the WB north of the Equator leads to a westward pressure gradient there and a lighter column south of the Equator leads to an eastward pressure gradient, as indicated by the arrows going into and out of the page. The AMOC lower limb, indicated by a homogenous field of identical southward velocities, is subject to a Coriolis force that is balanced by the zonal pressure gradient. The bulk of the AMOC lower limb takes place over a depth range D, defined as the vertical thickness of the AMOC lower limb.

Assumptions and approximations

We use the following assumptions and approximations for the Atlantic at low latitudes:

1. Pressure gradients and velocities become small on the interface h, as explained above.

2. The AMOC lower limb is contained within a zonally narrow strip along the WB, and $u << v$ so that $u \approx 0$. As a result, viscous effects are only due to gradients in v: we neglect the second order spatial derivatives of u. We also neglect $\frac{\partial^2 v}{\partial y^2}$.

3. We approximate the weakly stratified NADW between 1200-2400m depth by a homogeneous water mass.

4. Vertical NADW recirculation inside the Atlantic basin is small relative to AMOC lower limb.

5. Variations in h are small compared to the total outflow depth D.

6. Finally, this is not an assumption but a definition, we limit our focus to the AMOC lower limb. This depth range is located above the zero-streamline delineating the AABW and the NADW in the meridional stream function (Fig. 1). Velocities below the zero contour are

considered 0 in the analytical model, as they are not counted as NADW flow.

Assumption 1 is trivial in the ocean interior away from the WB, where pressure gradients and velocities are generally small. Assumption 3 implies a rapid density transition of negligible thickness across the level of no motion between the AAIW and NADW flows. The veracity of assumption 2 can also be judged from Fig. 2, assumption 4 from Fig. 1 and assumption 6 from Fig. 3.

Solutions to the equations of motion

The opposite moving Atlantic NADW and AAIW water masses (Fig. 1) are separated by a surface of no motion and negligible horizontal pressure gradients (assumption 1). Neglecting stratification inside the NADW column (Assumption 3) and assuming cancellation of the ocean surface gradients by the intervening baroclinic gradients at h (Assumption 1), we can express the horizontal pressure gradient $\frac{\nabla_H p}{\rho_0} = \frac{g\Delta\rho\nabla_H h}{\rho_0} \equiv g'\nabla_H h$, where $g' \equiv \frac{g\Delta\rho}{\rho_0}$ is the reduced gravity, and $\Delta\rho$ the density difference between the NADW and AAIW and ρ_0 is an average ocean density. The gradient ∇_H denotes the horizontal gradient $(\frac{\partial}{\partial x}, \frac{\partial}{\partial y}, 0)$. In our experiments $\rho_0 = 1035 kg/m^3$ and in our standard experiment $\Delta\rho = 0.33 kg/m^3$. A more complete discussion can be found in Appendix 1, where the underlying assumptions are specified and a mathematical derivation is given.

We now seek to relate the flow in the deep western boundary current below the interface to the horizontal gradient of h. The southward NADW flow is contained within a WBC of relatively small width, in which the meridional velocity v dominates the zonal velocity (Assumption 2) and the meridional velocity has only weak meridional variations. Neglecting the stratification inside the NADW column underneath h (Assumption 3) leads to an approximation of the flow by a vertically constant velocity there. Our focus is on the low latitudes, so we make the beta plane approximation. Omitting momentum advection and assuming a steady state, the equations of motion for the horizontal velocities at each depth in the NADW depth range are then:

(1) $$0 = \frac{\partial u}{\partial t} = \beta y v - g' \frac{\partial h}{\partial x}$$

(2) $$0 = \frac{\partial v}{\partial t} = A_H \frac{\partial^2 v}{\partial x^2} - \beta y u - g' \frac{\partial h}{\partial y}$$

where β denotes the value of $\frac{\partial f}{\partial y}$ at the equator, and f is the Coriolis parameter, now approximated by βy. Note that we assume $u = 0$, so that the viscous term balances the meridional pressure gradient in Eq. 2.

A detailed derivation of solutions for (u, v) and h to the equations of motion (Eqs. 1, 2) are given in Appendix 2. The equations of motion suggest a close correspondence between v and h, and trying a separable solution for h gives:

(3) $$h(x, y) = \bar{h} + y\ s_y e^{-\alpha x} (\frac{\sqrt{3}}{3} sin(\sqrt{3}\alpha x) + cos(\sqrt{3}\alpha x))$$

(4) $$v(x, y) = -\frac{4}{\sqrt{3}} s_y \alpha\ \frac{g'}{\beta}\ e^{-\alpha x} sin(\sqrt{3}\alpha x)$$

(5) $$M = \frac{gD}{\rho_0 \beta} s_y \Delta\rho$$

where $\alpha = \sqrt[3]{\frac{\beta}{8A_H}}$ (see Appendix 2) and M denotes the NADW outflow. Note that this solution requires $u = 0$. If A_H is known, the surface h is fully determined by specifying the average depth $\bar{h}$ and s_y. Note that h is linear in y when x is held constant, as s_y is a constant. Note also that M is also expressed in terms of quantities that can be easily determined from the GCM. We will later determine how well these equations approximate our numerical model. The damped oscillation in x in Eq. 3 is reminiscent of the x-dependence of pressure in the analytical solution for a zonal section of the Pacific deep western boundary current of Warren (1976). However, he examined only one latitude so that the meridional density structure and the role of the meridional pressure gradient could not be incorporated in that study.

Comparison of analytical solutions with the GCM

To give a general impression of the approximations we used in the analytic model, Figure 5a shows a vertical profile of velocity at 8.1 °N for the western-most Atlantic v in the GCM. This idealised profile, taking the form of a rectangular (step) function, arises from the idealisation of the density field at the western boundary (Fig. 5b) shown in Fig. 5c (Assumption 3). The density contours are more tightly packed around the interface h than inside the NADW water mass (Fig. 5b). Note that we omit density contours in the upper (light) part of Fig. 5b, as they are too tightly packed to be legible. The non-zero velocities below the rectangular function generally belong to the AABW cell underlying the AMOC lower limb (Fig. 1), and are subject to different dynamics than those described in this paper (e.g. Kamenkovich and Goodman 2000). In model configurations where AABW is absent, the space below the rectangular function could be regarded as the ocean floor. Falling outside the scope of our analysis, no density is assigned to it in Fig. 5c (Assumption 6).

In the analytic model, we calculate v from Equation 4, taking from the numerical model $s_y = \frac{\Delta h}{\Delta y}\Big|_{WB}$ with the change Δ taken between 10 °S and 10 °N and $\bar{h} = h(0,0)$. Equation 1 implies that, in the y-direction, the velocity equals the geostrophic velocity; $v = v_{geos}$. To examine how well $v = v_{geos}$ holds in the numerical model, Figure 6a shows the quotient v_{geos}/v at the Atlantic western-most Atlantic grid cell (where the strongest deviation from geostrophy might be expected, as viscous interaction with the WB is strongest here). This quotient is mostly very close to 1, indicating an excellent agreement. However, there is some discrepancy between v_{geos} and v immediately south of the equator, although also there the discrepancy is smallest at the core of the AMOC lower limb (with a maximal value around 10-15 percent). This could be related to f being small near the Equator, leading to an inaccurate calculation. Note that the discrepancies are generally smallest in the NADW core, where most of the kinetic energy is dissipated (Fig. 6b, c; see below). In conclusion, $v = v_{geos}$ holds well in the GCM at the WB. As a result, only the longitudinal variations of v can significantly contribute to viscous dissipation (Eq. 2).

The solution for v shown in Equation 4 is independent of y, with v constant along the WBC and small in the interior. For this to be the case in the GCM, as anticipated by the analytic model, the dashed curve in Fig. 7, representing h along a latitudinal section away from the WB (5 °to the east in this case), is horizontally flat, while h at the WB $h(0, y)$ is approximately linear with positive slope (solid curve). The interface h lies inside a vertical interval of low velocities (Fig. 7a) and pressure gradients (Fig. 7b), in accordance with Assumption

1.

The twisted interface h is associated with a relatively homogeneous southward flow below it (Fig. 7a). The Coriolis force on this flow is balanced by the pressure gradient below h shown in Fig. 7b. Importantly, the western boundary section $h(0, y)$ of h crosses the average depth value (approximated by the shown isopycnal at 5 °E of the western boundary) at the Equator $y = 0$, leading to a zonal pressure gradient reversal underneath (Fig. 7b). These elements are also indicated in the cartoon diagram in Fig. 4.

To examine whether $\frac{\nabla_H p}{\rho_0} = g'\nabla_H h$ is an appropriate approximation to the GCM, Figure 8 shows the interfacial isopycnal depth h in the GCM, zonal pressure gradient obtained directly from the GCM and the zonal pressure gradient calculated from h. As said, here we use $\Delta\rho = 0.33kg/m^3$, diagnosed by taking the density difference between 2000m depth (NADW) and 1000m depth (AAIW) at the Equator. There is a good agreement between the GCM pressure gradient (Fig. 8c) and that calculated via $\frac{1}{\rho_0}\frac{\partial p}{\partial x} = g'\frac{\partial h}{\partial x}$ (Fig. 8d).

The analytical interface h obtained from Eq. 3 shown in Fig. 8a compares favourably with h obtained from the GCM (Fig. 8b). In both cases, h shoals north of the Equator in the WBC region, and deepens to the south, and values close to $\bar{h}$ are attained near the Equator. The interior away from the WB remains relatively horizontal compared to the WBC region in both cases, with smaller undulations. Deepening of h associated with zonal flow further away from the Equator is present in the GCM, especially in the north-east corner, but absent in the analytical solution, indicating the limited validity of our approach there.

To further compare the analytically determined h and the underlying v with the GCM, Figures 9 and 10 show zonal profiles near the WBC of h and v at 3 different latitudes and 2 depths. Again, the analytical solutions do not yield $\bar{h}$, so this value has to be specified. As done above, $\bar{h}$ has been taken as the value of h at the western boundary at the Equator. We checked that similar results to those shown here are obtained for alternative definitions of $\bar{h}$, where we chose $\bar{h}$ inside the ocean interior away from the WB at the latitude of the zonal profile (figure not shown), as h is close to its average value also there. Also as above, the value of s_y has been determined as $s_y = \frac{\Delta h}{\Delta y}$, where the change in quantities $\Delta(y, h)$ is taken between 10 °S and 10 °N in latitude. Again, similar results are obtained for variations of this latitudinal domain, provided it remains contained inside the low latitudes. There is a very good agreement between the numerical model and the analytical model for the zonal profile of h and v at 8.1 °N (Fig. 9 left column) and 8.1 °S (Fig. 10a,b,c), although velocity agrees somewhat less at the deeper level $z = -2100m$ in the southern case (Fig. 10b). Reasonable yet reduced agreement is found further away from the Equator at 20.7 °N (Fig. 9b,d,f), indicating that the approximation works best near the Equator. The very good agreement of the width of the profile near the Equator lends credence to the formula $\alpha = \sqrt[3]{(\frac{\beta}{8A_H})}$ there. The overshoot to positive values in v (GCM) away from the western boundary is also present in both the numerical model and the analytical solution (e.g. Fig. 9c). The slope $\frac{\partial h}{\partial x}$ becomes 0 at the western boundary in the analytical solution to allow $v = 0$ there. This feature is absent in the numerical result, as it falls below the model resolution. Nonetheless, the western-most v attains a similar value to the y-component of the geostrophic velocity in the numerical model (see above).

AMOC under varying forcing.

Figure 11 shows the NADW outflow (at 32 °S), M, for eight other experiments with the GCM where we have changed the atmospheric moisture diffusivity (see Section 2) so as to achieve different overturning rates in response to altered buoyancy fluxes, in order to test the general applicability of the analytic description. In each experiment, the model was integrated for more than 6000 years in order to attain a steady state. The hydrological cycle is meridionally asymmetric in our model, and enhancing moisture diffusivity leads to greater freshwater transport to the Southern Ocean (see Saenko and Weaver 2003; Sijp and England 2008). Increases in the product $s_y \Delta\rho$ (via increasing moisture diffusivity) leads to increased NADW outflow M in the numerical model (Fig. 11b), and a generally good agreement is maintained between the numerical model and M calculated from Equation (5). In each instance the same procedure was followed to obtain s_y. We used D=1200m for the NADW outflow depth, instead of the full 1500m, to account for the vertical ramping of v at the water mass boundary. This procedure may need to be more flexible under extreme changes in the model as M depends on both $\Delta\rho$ and s_y. Both factors contribute to the increase in M (Fig. 11a). Included in the eight experiments are two where the moisture diffusivity field has been replaced by a spatially constant field (as in Sijp and England 2008). These are the two experiments with lowest rates M (the two left-most points in Fig. 11b), where a spatially constant moisture diffusivity of $10^6 m^2/s$ leads to $M = 7.8Sv$ and a diffusivity of $0.8 \times 10^6 m^2/s$ to $M = 6.8Sv$. Interestingly, the difference in M between these two experiments arises almost solely from a difference in slope s_y.

Energetics

The equations of motion yield the time evolution of kinetic energy density e_{kin} via multiplication by v, giving $\frac{\partial e_{kin}}{\partial t} = \rho_0 v \frac{\partial v}{\partial t} = \rho_0 v\ \kappa \frac{\partial^2 v}{\partial x^2} - \rho_0 g' v\ \frac{\partial h}{\partial y} = \rho_0 A_H \frac{\partial}{\partial x}(v \frac{\partial v}{\partial x}) - \rho_0 A_H (\frac{\partial v}{\partial x})^2 - \rho_0 g' v\ \frac{\partial h}{\partial y}$. The first term of the last expression is a divergence and can be recognised as the zonal transport of kinetic energy by viscous forces. The viscous KE transmission is mostly zonal and confined inside the western boundary (and so vanishes in the zonal integral), and the advection of KE is negligible (as in Gregory and Tailleux 2011). The second term, $-\rho_0 A_H (\frac{\partial v}{\partial x})^2 = -4\rho_0 A_H v_0^2 \alpha^2 e^{-2\alpha x} sin^2(\sqrt{3}\alpha x + \frac{2}{3}\pi)$, is the rate of viscous dissipation of energy per unit volume. The third term is the rate of potential energy conversion derived from the sloped overlying surface h. This term is the rate of work done by the pressure gradient inside the NADW water column. In steady state $\frac{\partial e_{kin}}{\partial t} = 0$, yielding a budget for the conversion of potential energy into kinetic energy and then into heat by viscous dissipation.

Zonal integration over the WBC domain leaves only the integrals of the viscous dissipation rate term $\rho_0 A_H (\frac{\partial v}{\partial x})^2$ and the potential energy conversion rate $-\rho_0 g' v \frac{\partial h}{\partial y}$, as the transport term vanishes. This means that although the component v (but not the vector (u,v)) satisfies the geostrophic equation, the strong zonal gradient in v near the western boundary allows for the conversion of potential energy derived from the meridionally sloped surface h into heat via viscous dissipation. Locally, the two processes are linked via zonal viscous energy transport. This situation is shown in Figure 10d, where the energy rate terms are shown. Potential energy is converted into kinetic energy near the core of the current, while viscous zonal energy transport allows this energy to be dissipated viscously close to the western boundary, where the gradient in v is the largest. A small amount of this energy is also transported to the opposite shoulder away from the western boundary, where the gradient in v is also large. Gregory and Tailleux (2011) describe the conversion of work done by the pressure gradient into kinetic energy and then heat via viscous dissipation in the HADCM3 and FAMOUS models. Their Figure 4 shows that work done by the pressure gradient is balanced by viscous dissipation, and that dissipation via horizontal diffusion dominates wherever pressure gradient work is positive. This is in agreement with our results. As in Gregory and Tailleux (2011), the pressure gradient is allowed to do work as it is not entirely perpendicular to the velocity due to vanishing u. In the present analytical model, deviation from geostrophy is only due to viscous effects allowing $u = 0$, a small effect. Gregory and Tailleux (2011) argue that even though departure from geostrophy is usually small, it is nevertheless essential for the energy budget of the oceans, as it is the term responsible for the conversion of potential energy into kinetic energy all the way along the western boundary.

Interestingly, the potential energy is converted from the meridional slope. Although one can determine v from the zonal slope $\frac{\partial h}{\partial x}$, this tells us little about what physical processes determine or limit v. In contrast, the fact that potential energy is converted from the meridional slope of h (and due to the $\Delta\rho$ across it) allows a statement about what global factors determine v, namely a portion of the rate of potential energy generation across the basin. Although this is consistent with the view recently advocated by Tailleux (2009) and Hughes et al. (2009), it is difficult to infer overturning strength from global energy budgets here. We make no attempt to determine this portion from the global energy budgets, and only state that once available, s_y and $\Delta\rho$ are such that the rate is proportional to $(s_y\Delta\rho)^2$, and therefore always positive. Interestingly, the latter quantity is similar to the expression for the available potential energy in a two-layer model separated by a horizontally sloping interface, yielding a further connection to APE theory. We therefore find that the meridional gradient of h and the density difference across it is a more fundamental determinant of v than the zonal gradient, while the zonal pressure gradient adjusts in response and so yields no information about what sets v.

We can express the zonally integrated energy dissipation rate density ("energy dissipation" for short) in terms of the velocity. Recall from Appendix 2 that $V(y,z) \equiv \int_0^\infty v \,\mathrm{d}x = \frac{v_0\sqrt{3}}{4\alpha}$ (where we take $x = 0$ at the western basin margin). Then, the energy dissipation is $W(y,z) \equiv \int_0^\infty \rho_0 A_H (\frac{\partial v}{\partial x})^2 \,\mathrm{d}x = 4\rho_0 A_H \alpha^2 v_0^2 \int_0^\infty e^{-2\alpha x} sin^2(\sqrt{3}\alpha x + \frac{2}{3}\pi)\,\mathrm{d}x = \frac{3}{4}\rho_0 A_H \alpha v_0^2$. Here, we have used $\int_0^\infty e^{-2\alpha x} sin^2(\sqrt{3}\alpha x + \frac{2}{3}\pi)\,\mathrm{d}x = \frac{3}{16\alpha}$.

Substituting v_0 and recalling (Appendix 2) $\alpha^3 = \frac{\beta}{8A_H}$, we obtain:

(6) $$W = \frac{1}{2}\rho_0 \beta V^2 = \frac{3}{2}\frac{g^2}{\rho_0 \beta}\Delta\rho^2 s_y^2$$

The energy dissipation calculated from model data using (6) is shown in Figure 6c, and compares reasonably well with the energy dissipation calculated via the rate of work done by the pressure gradient, $-\nabla p \cdot \mathbf{v}$ (Fig. 6b). This lends support to our energy analysis. The energy dissipation is confined to the low latitudes where our approximation works best, rendering our framework a good tool for calculating the total energy dissipation associated with the lower limb of the AMOC. Equation 6 also suggests that $W \propto M^2$. Note that W depends on β, suggesting that energy dissipation depends on the rotation rate, and its local rate of change with latitude.

Undulations in h are associated with available potential energy that could be released by pressure work arising from the ensuing pressure gradients. Unlike a non-rotating case, the meridional slope of h near the WB is the only slope from which the available potential energy can be released in this manner. This work is done in the lower limb of the AMOC mostly at the latitudes where our approximation is most valid, yielding an estimate of the energy dissipation rate associated with this flow. The creation of the available potential energy is associated with diapycnal mixing, wind stress and surface buoyancy forcing (Hughes et al. 2009). The precise energy pathways leading to the potential energy tied up in the meridional slope of h at the WB are diverse and beyond the scope of this study, although we can already say that buoyancy forcing changes that increase $\Delta\rho$ would also increase the work done by the meridional pressure gradient field, and so the energy dissipation rate. This is then associated with a stronger AMOC. Also, a deeper $\bar{h}$ would likely yield a larger s_y, as h remains constrained by its outcrop region in the north, leading to a higher energy dissipation rate and stronger flow. The available potential energy related to h in the Atlantic is related to its average depth h, which in turn is strongly related to the depth of h at 32 °S, a value that is influenced by the SH westerlies. Local wind stress also constrains the shape h at the northern outcrop regions by steepening isopycnals there, suggesting an role for both basin-scale wind stress and buoyancy forcing in determining s_y. Also, the steepening of h near its outcrop region suggests that the average depth $\bar{h}$ determines an upper bound s_y^{max} to s_y, namely $S_y^{max} = \bar{h}/L^y$, where L^y is the distance between the equator and the latitude of the North Atlantic outcrop region of h. This also yields an upper bound for M and the potential energy that can be converted from h (via pressure work), provided $\Delta\rho$ remains constant. Finally, eddies remove potential energy by flattening h via the GM parameterisation. This effect is strongest in the SO, and less important inside the basin (Kamenkovich and Sarachik 2004).

4. Summary and Conclusions

We have proposed a new analytical description of the AAIW-NADW interface h and the underlying DWBC at low latitudes. This has allowed us to understand the processes limiting the NADW outflow rate, and the mechanisms that make the flow locally dependent on the AAIW-NADW density difference. Our approach works best near the Equator (e.g. between 10 $^\circ$S and 10 $^\circ$N), and becomes somewhat less accurate at high northern latitudes and around 30 $^\circ$S. Nonetheless, the low latitude validity of the description allows us to obtain a more general scaling for the NADW outflow rate M, as the flow must pass the low latitudes to exit the basin. Our approximation to the vertical profile of v is a Heaviside function, whereas the GCM exhibits a more gradual profile sculpted by further subtle density transitions inside the NADW column. Despite the simplicity of this approximation, a function for M in terms of $s_y\Delta\rho$ is obtained that compares very favourably to the GCM. We offer no precise description of how buoyancy forcing affects the density field, although this will be needed in a future study to link the overturning to surface forcing. Finally, our approach does not capture the underlying AABW cell and does not yield an expression for the NADW column thickness D. Instead, this must be estimated from the GCM output. Furthermore, no description is offered of the upper branch of the AMOC.

A brief energy analysis shows that potential energy arising from the meridional slope of h is converted into kinetic energy and then viscously dissipated. This yields a constraint on the flow, namely the rate of basin-wide potential energy production via this slope. In contrast, the zonal slope is a passive response arising from a geostrophic adjustment mechanism, perhaps similar in essence to that described in Johnson and Marshall (2002). Indeed, the deep meridional velocity can be derived from the zonal pressure gradient via a thermal wind balance, but this procedure yields no information about the driving mechanisms maintaining this dissipative flow. Gregory and Tailleux (2011) also emphasise the role of this energy conversion process in limiting the NADW overturning rate. The analytical expression for h (Eq. 3) provides a relationship between the zonal and meridional pressure gradient.

Scaling of the upper limb of the AMOC generally involves linking zonal to meridional pressure gradients and velocities, and employ basin-wide zonal scales (see De Boer et al. 2010, for a discussion). In contrast, we show here that the zonal scales of these quantities are the WBC width for the AMOC lower limb. Here, the AMOC is described as a dissipative system largely confined to the western boundary region, where available potential energy associated with local density structure is converted into kinetic energy, yielding a constant velocity subject to viscous drag at each latitude. This suggests the importance of future investigation of the relationship between this study and the studies by Hughes et al. (2009) and Tailleux (2009), who stress the importance of available potential energy in facilitating the transfer of kinetic energy to the background potential energy in maintaining the AMOC, and that the rate of transfer between different energy reservoirs is more important than the total available potential energy.

Our deep circulation differs from that proposed by Stommel and Arons (1960), who assume a uniform abyssal upwelling across the Atlantic thermocline base. In contrast, we assume little or no low-latitude Atlantic upwelling, as in observations (Talley et al. 2003) and our numerical model (see Section 2). Also, the horizontal abyssal recirculation characteristic of the Stommel and Arons (1960) model is absent in our numerical model (Fig. 2) and analytical model. The Stommel and Arons (1960) approach regards the DWBC as a passive response to the introduction of a mass source (deep sinking) in the deep layer located in the North Atlantic. In contrast, in our approach the DWBC is coupled to the overlying interfacial surface h, and both interact to evolve to a steady state.

Our experiments take place in a flat bottom idealised numerical model below eddy permitting resolution, yielding a relatively quiescent deep circulation away from the western boundary. In contrast, several recent observational studies find that subsurface floats injected within the DWBC of the Labrador Sea are commonly advected into the North Atlantic deep interior, in apparent contrast to the view that the deep water formed in the North Atlantic predominantly follows the DWBC (e.g. Bower et al. 2009; Lozier 2010). Indeed, in the ocean eddy-permitting model of Spence et al. (2011), a portion of NADW separates from the western boundary and enters the low-latitude Atlantic via interior pathways distinct from the DWBC, with a the total southward transport off shore of the DWBC of about 5Sv at 35 °N. However, unlike the model used in the present study, that study employs also a detailed ocean bathymetry while the present study seeks to isolate the AMOC scaling factors in a simple setting. Furthermore, the NADW recirculation described in Spence et al. (2011) takes place at or to the north of our domain of interest while, as in our study, southward flow is the norm within most of the low latitudes also in their model. Also, our approach assumes a dominant role for the viscous dissipation of momentum in the horizontal direction, whereas in the real system bottom pressure torques may play a significant role (Hughes and de Cuevas 2001). However, the results discussed here apply to non-eddy resolving models, and provide a better understanding of their behaviour. Furthermore, the details of the energy dissipation can be adjusted in our framework.

De Boer et al. (2010) find that the AMOC scale depth is set by the depth of the maximal AMOC streamfunction, instead of the pycnocline depth, and emphasise that these depths differ. This is in agreement with our experiments, as $\bar{h}$ represents this scale depth. However, although the meridional slope s_y of h at the western boundary is related to $\bar{h}$ because h must outcrop near the northern boundary, we find no direct or simple way to link s_y to $\bar{h}$. This is because the slope $\frac{\partial h}{\partial y}$ is only constant along the boundary at low latitudes, and increases sharply north of 50 $^{\circ}$N. There is an indirect link, as deepening of $\bar{h}$ would yield greater isopycnal slopes near the northern boundary, and therefore more available potential energy. The availability of this extra potential energy to the AMOC then determines how s_y increases with $\bar{h}$. Processes influencing $\bar{h}$ take place in the Southern Ocean (e.g. Gnanadesikan 1999) as well as via diapycnal mixing and the horizontal distribution of buoyancy at the ocean surface, thus supplying energy to the deep WBC and determining outflow rates. Furthermore, AABW constrains the vertical extent D of the AMOC lower limb as well as influencing h, providing a further constraint.

We determine the constants needed in our M scaling more directly from our numerical model so that we can verify our formula against numerical model results without tuning the result to fit the overturning rate or deep velocities, yielding a good validation of our analytical model. Nonetheless, our basin-geometry is rectangular, and our approach may require the introduction of further geometrical factors in models with a more realistic and irregular geometry. Furthermore, geometrical factors enter our considerations via the choice of location where we conduct our analysis (low latitudes) and the depth-range D of the NADW outflow. Nonetheless, we provide further insight into the origins of geometrical constants and provide a scaling where factors can be obtained from GCM output (Eq. 6). We link this to the local mechanisms at play in driving the NADW outflow. The depth of the NADW outflow, the density difference between the stacked water masses and the meridional slope of their interface at the western boundary need to be determined to yield the NADW outflow rate.

Appendix 1. Vanishing pressure gradient on interface h

We examine an isopycnal surface h of density ρ_h situated between the tongues of AAIW and NADW moving in opposite directions. These flows are essentially pressure-driven (see also Gnanadesikan 1999), and h resides inside a depth range where velocities and pressure gradients are small (see Fig. 7b). We assume the ocean is in hydrostatic balance i.e. $\frac{\partial p}{\partial z} = -g\rho$ for z increasing in the upward direction and zero at the sea surface, where p is pressure,

g gravity and ρ ocean density. Therefore, $\frac{\partial \nabla_H p}{\partial z} = -g \nabla_H \rho$, yielding $\nabla_H p(z) = \nabla_H p_0 + g \int_z^0 \nabla_H \rho(\tilde{z}) \, \mathrm{d}\tilde{z}$, where $\nabla_H p_0$ is the rigid lid pressure gradient at the lid surface $z = 0$. The gradient ∇_H denotes the horizontal gradient $(\frac{\partial}{\partial x}, \frac{\partial}{\partial y}, 0)$. We will only be concerned with horizontal pressure gradients and velocities, as isopycnal slopes are very small in our region of interest, and the horizontal velocity scale generally exceeds the vertical velocity scale by a factor of 10^4. The interface depth h is simply such that $\nabla_H p = 0$ at $z = h$ (Assumption 1), so for any $z < h$, $\nabla_H p(z) = \nabla_H p_0 + g \int_h^0 \nabla_H \rho(\tilde{z}) \, \mathrm{d}\tilde{z} + g \int_z^h \nabla_H \rho(\tilde{z}) \, \mathrm{d}\tilde{z} = g \int_z^h \nabla_H \rho(\tilde{z}) \, \mathrm{d}\tilde{z}$. Hence the geostrophic velocity $v(z) = 1/f\rho_0 \, \partial p/\partial x = g/f\rho_0 \int_z^h \, \partial\rho/\partial x \, dz$, and similarly for $u(z)$.

Now, along an isopycnal surface z_ρ of density ρ, we have: $\frac{\partial \rho}{\partial x} dx + \frac{\partial \rho}{\partial y} dy + \frac{\partial \rho}{\partial z} dz = 0$, so $\frac{\partial \rho}{\partial x} = -\frac{\partial \rho}{\partial z} \frac{\partial z_\rho}{\partial x}$, where z_ρ denotes the depth of the isopycnal of density ρ. Then

$$v(z) = -\frac{g}{\rho_0 f} \int_z^h \frac{\partial \rho(\tilde{z})}{\partial z} \frac{\partial z_\rho}{\partial x} \, \mathrm{d}\tilde{z}$$

We now approximate the density distribution over $z \in [-\infty, h]$ as $\rho(z) = \rho_{NADW} - (\rho_{NADW} - \rho_{AAIW}) H(z - h)$, where H is the Heaviside function. Note that we generally take ρ_{NADW} to be the density at the western boundary, the Equator and 1800m depth (the core of the outflow). ρ_{AAIW} is defined at the same horizontal location at 1000m depth. This crude approximation to the density field amounts to assigning a single uniform density to the NADW water mass ρ_{NADW}, and assuming a relatively rapid density transition from ρ_{AAIW} to ρ_{NADW} across h (Assumption 3). Then, $\frac{\partial \rho}{\partial z} = -(\rho_{NADW} - \rho_{AAIW}) \delta(z - h)$, where δ is the Dirac delta function, and substituting this in the z-integral gives $v(z) = \frac{g}{\rho_0 f} (\rho_{NADW} - \rho_{AAIW}) \frac{\partial h}{\partial x} = \frac{g'}{f} \frac{\partial h}{\partial x}$ for $z < h$, where $g' = \frac{g \Delta \rho}{\rho_0}$ is the reduced gravity. We generally assume the beta plane approximation $f \approx \beta y$. We estimate an effective thickness D of about 1200m for the NADW outflow, leading to a maximal NADW outflow depth $h + 1200 \approx 2400m$. This choice can be regarded as a "geometrical factor" (see Introduction), and visual inspection of Fig. 1 suggests it is a reasonable choice. We ignore the contribution to the NADW outflow below this depth, as by definition the NADW flow resides above the zero contour (Fig. 1). We define $v = 0$ there for our purposes. In reality, further density gradients give rise to a reduction in flow below the NADW. The zonal maxima of the analytically determined meridional velocity generally coincide with v at the western-most Atlantic grid cell in the GCM (Fig. 9 and Fig. 10).

Appendix 2. Derivation of solution to equations of motion.

Here we derive useful solutions to the equations of motion Eqs. 1,2. We restate the equations in the more general form using f, and without the beta plane approximation used in the main text (the approximation will be introduced below):

(1')
$$0 = \frac{\partial u}{\partial t} = fv - g' \frac{\partial h}{\partial x}$$

(2')
$$0 = \frac{\partial v}{\partial t} = A_H \frac{\partial^2 v}{\partial x^2} - fu - g' \frac{\partial h}{\partial y}$$

Recall that $u \approx 0$, which will be used below. We cross differentiate the equations of motion to obtain the vorticity equation $-A_H \frac{\partial^3 v}{\partial^3 x} + \beta v + f(\frac{\partial u}{\partial x} + \frac{\partial v}{\partial y}) = 0$. Near the equator, where f goes to zero, the vorticity balance is well approximated by $\frac{\partial^3 v}{\partial^3 x} = \frac{\beta v}{A_H}$. Note also that the weak NADW recirculation in our model (Fig. 1, Assumption 4) renders the horizontal flow largely divergence-free inside the NADW depth range, also rendering the 3rd term small. Interestingly, this equation can be recognised as that governing the boundary-layer solution in Munk (1950)'s model of wind-driven circulation. The physically acceptable solution along the western boundary is simply given by $v = v_0(y)e^{-\alpha x} sin(\sqrt{3}\alpha x)\ \frac{g'}{\beta}$, where $v_0(y)$ is an undetermined function of y, and $\alpha = r_1/2 = \frac{1}{2}(\frac{\beta}{A_H})^{1/3}$. Note that v appears separable in x and y. This motivates writing $h = \bar{h} + F(x)G(y)$. F represents a longitudinal profile while G is the latitudinal amplification of this profile to satisfy geostrophy in Eq. (1'), where $G(0) = 0$. As we are only discussing the dynamics for the low latitudes, we shall now assume a β-plane approximation, and take for β its value at the Equator. Equations (1) and (2) indicates a close correspondence between the x-dependence of v and h, and trying $h(x, y) = \bar{h} + y\ s_y e^{-\alpha x}(\frac{\sqrt{3}}{3} sin(\sqrt{3}\alpha x) + cos(\sqrt{3}\alpha x))$ gives $v_0 = -\frac{g' s_y}{2\sqrt{3}A_H\alpha^2} = -\frac{4}{\sqrt{3}} s_y \alpha\ \frac{g'}{\beta}$ where s_y is simply the constant slope of h at the western boundary. It is likely determined by non-local factors. Also, $u = 0$ ($-\beta y u$ is the only y-dependent term in Eq. 2). The integrated transport in the boundary layer is therefore

$$V = v_0(y) \int_0^\infty e^{-\alpha x} sin(\sqrt{3}\alpha x)\, \mathrm{d}x = \frac{v_0(y)\sqrt{3}}{4\alpha} = -\frac{g' s_y \sqrt{3}}{\beta}$$

which is independent of A_H, as in Munk (1950). Note that here we take $x = 0$ at the western basin margin.

Multiplying V by the vertical extent of the NADW column D yields the NADW outflow. We thus assume that the variations in h are small compared to D. This yields Equations 3, 4 and 5.

Acknowledgements. We thank the University of Victoria staff for support in usage of their coupled climate model. This research was supported by the Australian Research Council and the Australian Antarctic Science Program. This research was undertaken on the NCI National Facility in Canberra, Australia, which is supported by the Australian Commonwealth Government. We thank Andreas Oschlies for hosting a visit to IFM-GEOMAR and supplying code and advice to allow W. P. Sijp to implement the turbulent kinetic energy scheme of Blanke and Delecluse (1993) based on Gaspar et al. (1990) into the model.

References

Blanke, B. and P. Delecluse, 1993: Variability of the tropical Atlantic ocean simulated by a general circulation model with two different mixed-layer physics. *J. Phys. Oceanogr.*, **23**, 13631388.

Bower, A., M. Lozier, S. Gary, and C. Boning, 2009: Interior pathways of the North Atlantic meridional overturning circulation. *Nature*, **459**, 243–248.

Bryan, F., 1987: Parameter sensitivity of primitive equation ocean general circulation models. *Journal of Physical Oceanography*, **17**, 970–985.

De Boer, A. M., A. Gnanadesikan, N. R. Edwards, and A. J. Watson, 2010: Meridional density gradients do not control the Atlantic overturning circulation. *Journal of Physical Oceanography*, **40**, 368–380.

Dijkstra, H. A., 2008: Scaling of the Atlantic meridional overturning in a global ocean model. *Tellus*, **60a**, 749–760.

Gaspar, P., Y. Gregoris, and J. M. Lefevre, 1990: A simple eddy kinetic energy model for simulations of the oceanic vertical mixing: Tests at station papa and long-term upper ocean study site. *J. Geophys. Res.*, **95**, 1617916193.

Gent, P. R. and J. C. McWilliams, 1990: Isopycnal mixing in ocean general circulation models. *Journal of Physical Oceanography*, **20**, 150–155.

Gerdes, R., C. Köberle, and J. Willebrand, 1991: The influence of numerical advection schemes on the results of ocean general circulation models. *Climate Dynamics*, **5**, 211–226.

Gnanadesikan, A., 1999: A simple predictive model for the structure of the oceanic pycnocline. *Science*, **283**, 2077–2079.

Gnanadesikan, A., A. M. de Boer, and B. K. Mignone, 2007: A simple theory of the pycnocline and overturning revisited. *Geophysical Monograph American*, **173**, 19–32.

Gregory, J. M. and R. Tailleux, 2011: Kinetic energy analysis of the response of the Atlantic meridional overturning to CO2-forced climate change. *Climate Dynamics (In Press)*, **-**, DOI 10.1007/s00382–010–847–6.

Griesel, A. and M. A. Morales-Maqueda, 2006: The relation of meridional pressure gradients to North Atlantic deep water volume transport in an ocean general circulation model. *Climate Dynamics*, **26**, 781–799.

Hughes, C. and B. de Cuevas, 2001: Why western boundary currents in realistic oceans are inviscid: a link between form stress and bottom pressure torques. *Journal of Physical Oceanography*, **31**, 2871–2885.

Hughes, G. O., A. M. C. Hogg, and R. W. Griffiths, 2009: Available potential energy and irreversible mixing in the meridional overturning circulation. *Journal of Physical Oceanography*, **39**, 3130–3146.

Hughes, T. M. C. and A. J. Weaver, 1994: Multiple equilibria of an asymmetric two-basin ocean model. *Journal of Physical Oceanography*, **24**, 619–637.

Johnson, H. and D. P. Marshall, 2002: A theory for the surface Atlantic response to thermohaline variability. *Journal of Physical Oceanography*, **32**, 1121–1132.

Kalnay, E., M. Kanamitsu, R. Kistler, W. Collins, D. Deaven, L. Gandin, M. Iredell, S. Saha, G. White, J. Woollen, Y. Zhu, A. Leetmaa, and R. Reynolds., 1996: The NCEP/NCAR 40-year re-analysis project. *Bull. Amer. Meteor. Soc.*, **77**, 437–471.

Kamenkovich, I. V. and P. J. Goodman, 2000: The dependence of AABW transport in the Atlantic on vertical diffusivity. *Geophysical Research Letters*, **27**, 3739–3742.

Kamenkovich, I. V. and E. S. Sarachik, 2004: Mecahnisms controlling the sensitivity of the Atlantic ThermohalineCirculation to the parameterization of eddy transports in ocean GCM. *Journal of Physical Oceanography*, **34**, 1628–1647.

Levermann, A. and J. J. Fuerst, 2010: Atlantic pycnocline theory scrutinized using a coupled climate model. *Geophysical Research Letters*, **37**, doi:10.1029/2010GL044180.

Levermann, A. and A. Griesel, 2004: Solution of a model for the oceanic pycnocline depth: Scaling of overturning strength and meridional pressure difference. *Geophysical Research Letters*, **31**, doi:10.1029/2004GL020678.

Lozier, M., 2010: Deconstructing the conveyor belt. *Science*, **328**, 1507–1511.

Manabe, S. and R. J. Stouffer, 1988: Two stable equilibria of a coupled ocean-atmosphere model. *Journal of Climate*, **1**, 841–866.

— 1999: Are two modes of thermohaline circulation stable? *Tellus*, **51A**, 400–411.

Marotzke, J., 1997: Boundary mixing and the dynamics of three-dimensional thermohaline circulations. *Journal of Physical Oceanography*, **27**, 1713–1728.

Munk, W. H., 1950: on the wind-driven ocean circulation. *Journal of Meteorology*, **7**, 3–29.

Pacanowski, R., 1995: *MOM2 Documentation User's Guide and Reference Manual: GFDL Ocean Group Technical Report 3*. NOAA, GFDL. Princeton, 3 edition, 232pp.

Park, Y. G. and J. A. Whitehead, 1999: Rotating convection driven by differential bottom heating. *Journal of Physical Oceanography*, **29**, 1208–1220.

Rahmstorf, S., 1996: On the freshwater forcing and transport of the Atlantic thermohaline circultion. *Climate Dynamics*, **12**, 799–811.

Robinson, A. R., 1960: The general thermal circulation in equatorial regions. *Deep-Sea Research*, **6**, 311–317.

Robinson, A. R. and H. Stommel, 1959: The oceanic thermocline and the associated thermohaline circulation. *Tellus*, **11**, 295–308.

Saenko, O. A. and A. J. Weaver, 2003: Atlantic deep circulation controlled by freshening in the Southern Ocean. *Geophysical Research Letters*, **30**, doi:10.1029/2003GL017681.

Schewe, J. and A. Levermann, 2010: The role of meridional density differences for a wind-driven overturning circulation. *Climate Dynamics*, **34**, 547–556.

Sijp, W. P. and M. H. England, 2004: Effect of the Drake Passage throughflow on global climate. *Journal of Physical Oceanography*, **34**, 1254–1266.

— 2008: Atmospheric moisture transport determines climaticresponse to the opening of drake passage. *Journal of Climate (submitted)*, **0**, 0.

Spence, P., O. Saenko, W. P. Sijp, and M. England, 2011: The role of bottom pressure torque on the interior pathways of NADW. *Journal of Physical Oceanography (accepted)*, **–**, –.

Stommel, H. and A. B. Arons, 1960: On the abyssal circulation of the world ocean, I. an idealized model of the circulation pattern and amplitude in oceanic basins. *Deep-Sea Res.*, **6**, 217–233.

Tailleux, R., 2009: On the energetics of stratified turbulent mixing, irreversible thermodynamics, boussinesq models, and the ocean heat engine controversy. *Journal of Fluid Mechanics*, **639**, 339–382.

Talley, L. D., J. L. Reid, and P. E. Robbins, 2003: Data-based meridional overturning streamfunctions for the global ocean. *Journal of Climate*, **16**, 3213–3226.

Thorpe, R. B., J. M. Gregory, T. C. Johns, R. A. Wood, and J. F. B. Mitchell, 2001: Mechanisms determining the Atlantic thermohaline circulation response to greenhouse gas forcing in a non-flux-adjusted coupled climate model. *Journal of Climate*, **14**, 3102–3116.

Vellinga, M. and R. A. Wood, 2002: Global climatic impacts of a collapse of the Atlantic thermohaline circulation. *Climate Change*, **54**, 251–267.

Warren, B. A., 1976: Structure of deep western boundary currents. *Deep-Sea Research*, **23**, 129–142.

Weaver, A. J., M. Eby, E. C. Wiebe, and co authors, 2001: The UVic Earth System Climate Model: model description, climatology, and applications to past, present and future climates. *Atmosphere-Ocean*, **39**, 1067–1109.

Wright, D. G. and T. F. Stocker, 1991: zonally averaged ocean model for thermohaline circulation. part i. model development and flow dynamics. *Journal of Physical Oceanography*, **21**, 1713–1724.

Wright, D. G., C. B. Vreugdenhil, and T. M. C. Hughes, 1995: Vorticity dynamics and zonally averaged ocean circulation models. *Journal of Physical Oceanography*, **25**, 2141–2154.

List of Figures

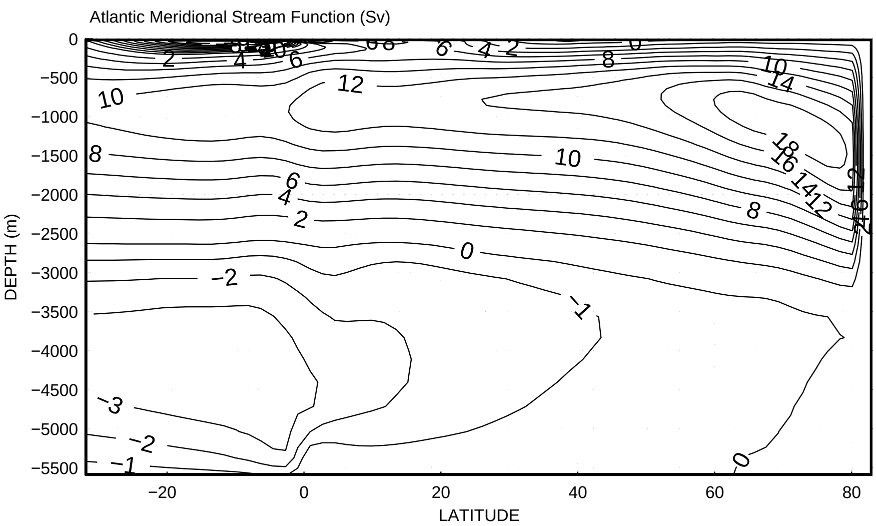

Figure 1: Atlantic meridional overturning streamfunction, 10 year average. Obtained via vertical integration of the basin-wide zonal integral of v. Positive values indicate clockwise flow. Values are given in Sv (1 Sv = 10^6 m^3 sec^{-1}).

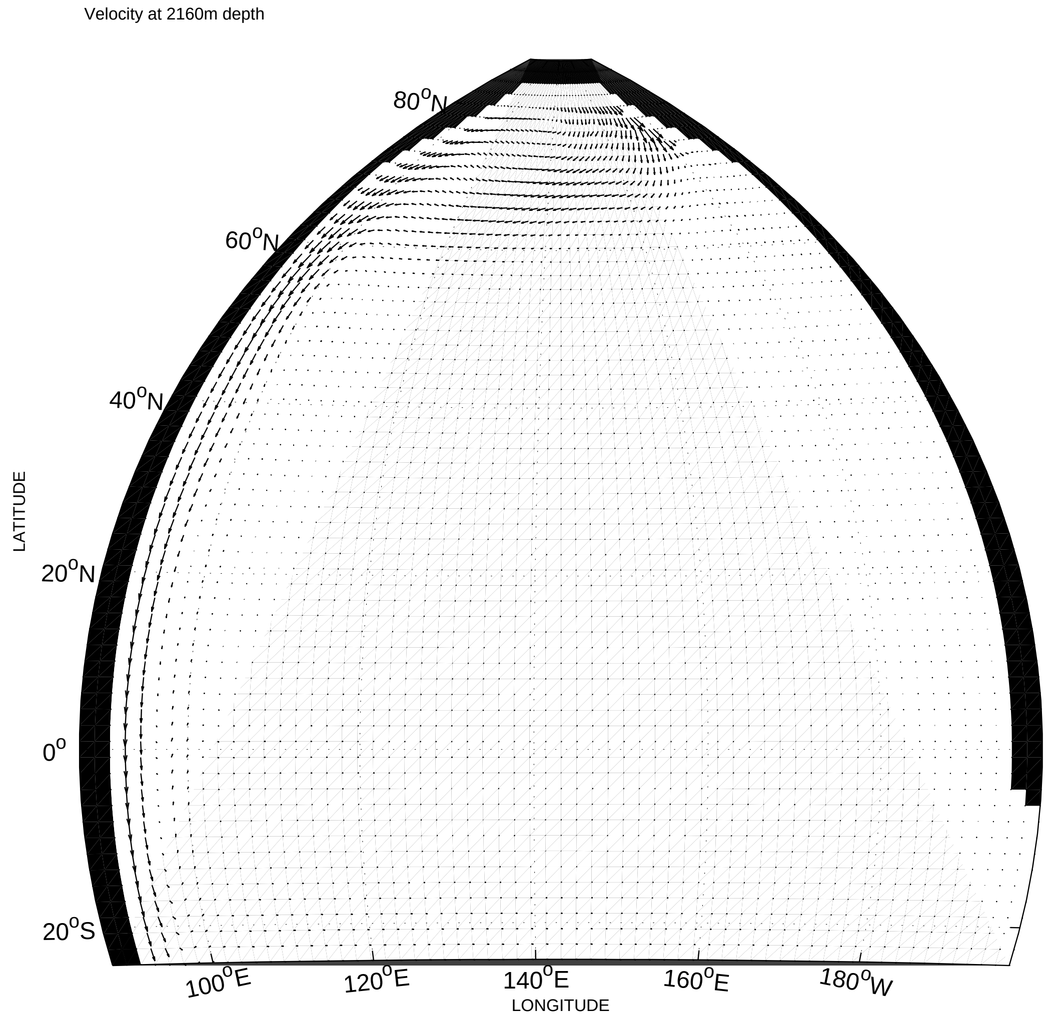

Figure 2: Direction of NADW flow at 2160m depth in the Atlantic. A typical velocity in the WBC is 3 cm/s. Taken from 10 year average.

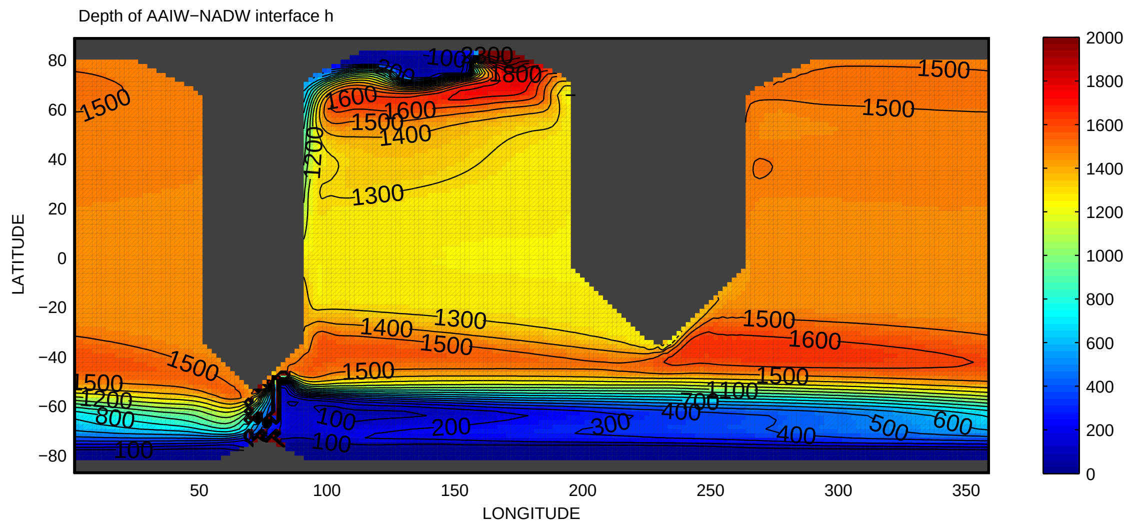

Figure 3: Depth of isopycnal h that lies between the AAIW and NADW tongues in the Atlantic (depth in m). The narrow basin displayed near the centre of the figure is identified with the Atlantic basin. We generally take $x = 0$ at the western boundary of this basin. Taken from 10 year average.

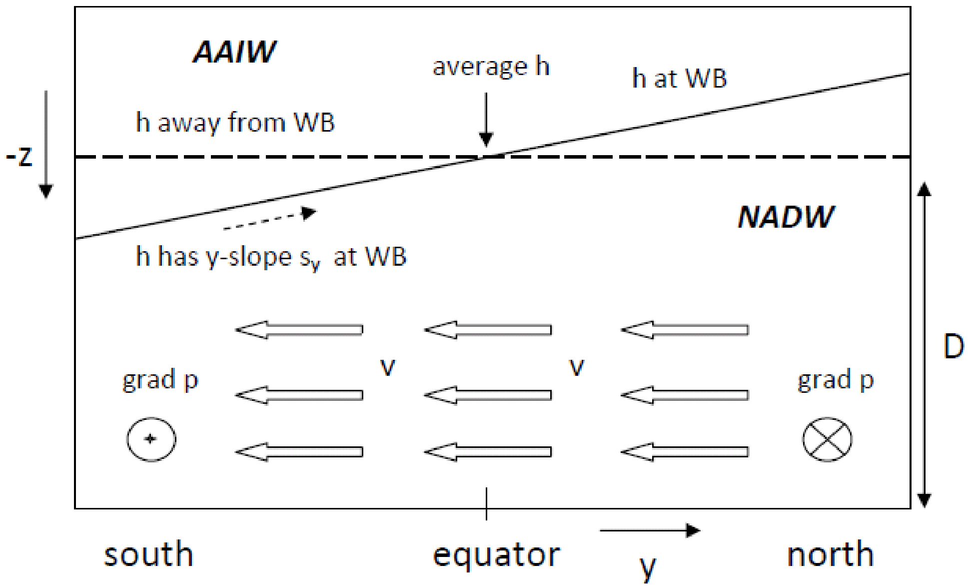

Figure 4: Schematic representation of AMOC lower limb and the AAIW-NADW interface h. The interface h assumes its average depth and has a very small latitudinal (y) slope in the interior away from the western boundary (dashed), and has a constantant positive latitudinal slope at the boundary (solid), where it attains its average value only at the equator (where the solid and dashed lines intersect). The vertical displacement of h from its average depth at the western boundary leads to a zonal pressure gradient and a meridional flow v, where the direction into the page is indicated by a cross inside a circle (x, on the right) and out of the page by a very small + inside a circle (on the left).

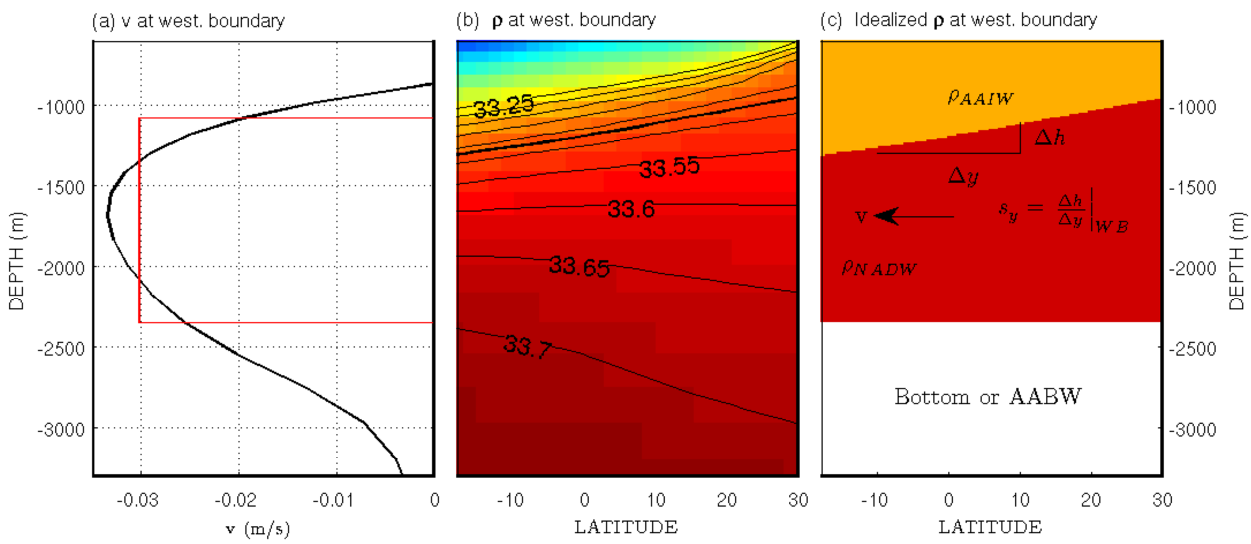

Figure 5: Values at the Atlantic western boundary grid cell of a) the meridional velocity v (m/s) at 8.1 °N where values from the numerical model are black and values from the analytical theory are red, b) σ (kg/m^3) with ρ referenced to 1200m depth and c) an idealization of the density at the western boundary. The interface h is indicated by a bold contour in (b). The idealization in (c) approximates σ in the NADW depth range by σ_{NADW} and σ above h by σ_{AAIW}. Taken from 10 year average.

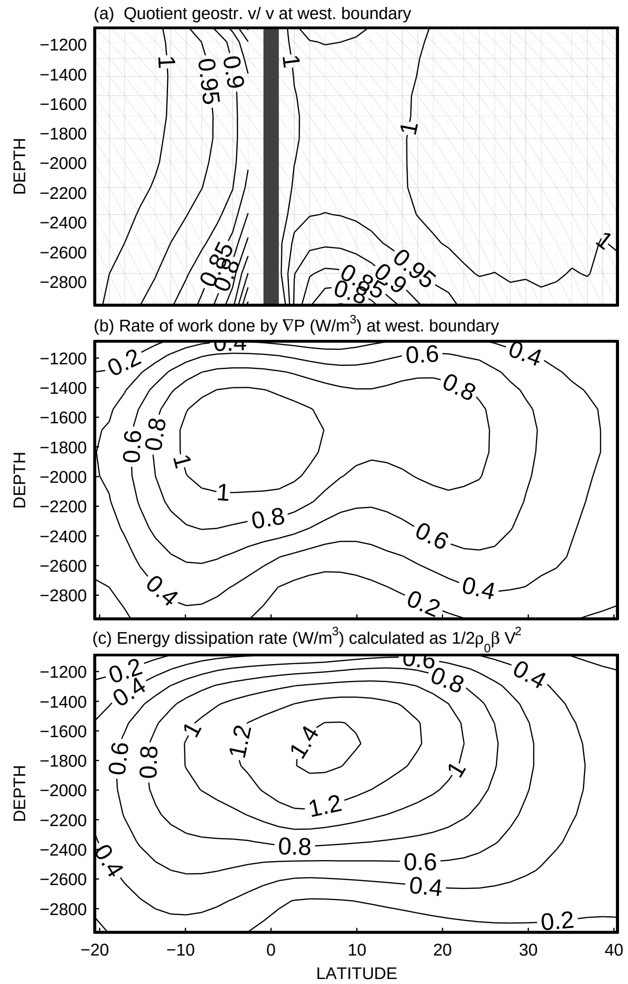

Figure 6: a) Atlantic western boundary grid cell values of geostrophic meridional velocity v_{geos} divided by the actual meridional velocity v in the model, $\frac{v_{geos}}{v}$. b) The zonal total of the energy dissipation rate density (W/m^2) calculated over the western boundary layer via work done by the pressure gradient, and calculated as the zonal integral of $\nabla p \cdot \mathbf{v}$. c) Same as (b), but calculated via $\frac{1}{2}\rho_0 \beta V^2$, where $V = \int_0^\infty v(x)\,\mathrm{d}x$. Note that we omit equatorial values of v_{geos}/v in (a), as f vanishes there.

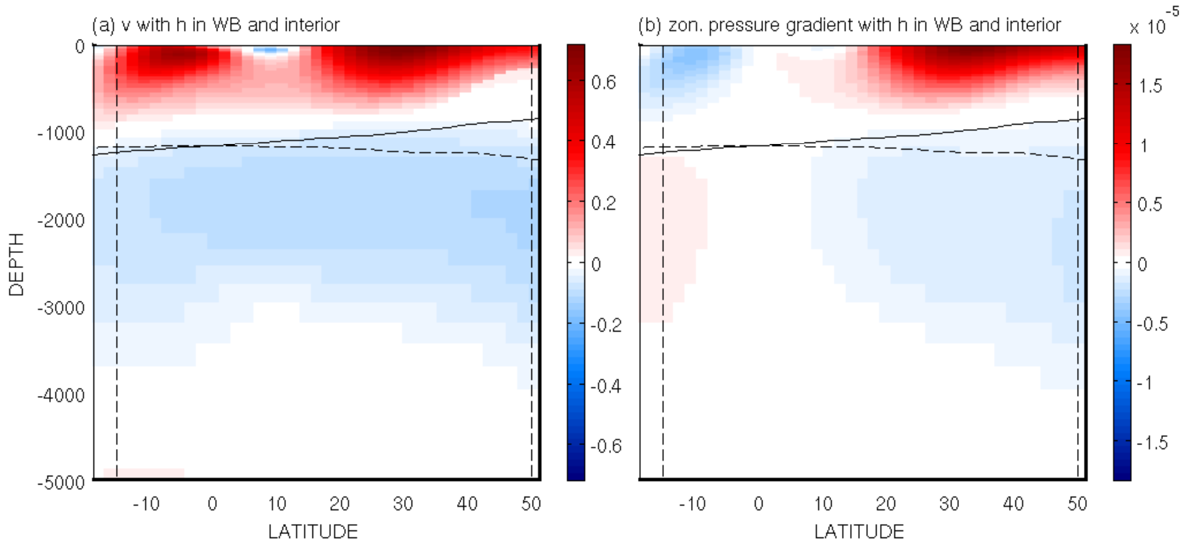

Figure 7: Values at western Atlantic boundary of a) meridional velocity v (m/s) and b) zonal pressure gradient (Pa/m). Overlaid are the depth of the AAIW-NADW interfacial isopycnal at the western boundary (solid) and 5 °longitude east of the western boundary (dashed).

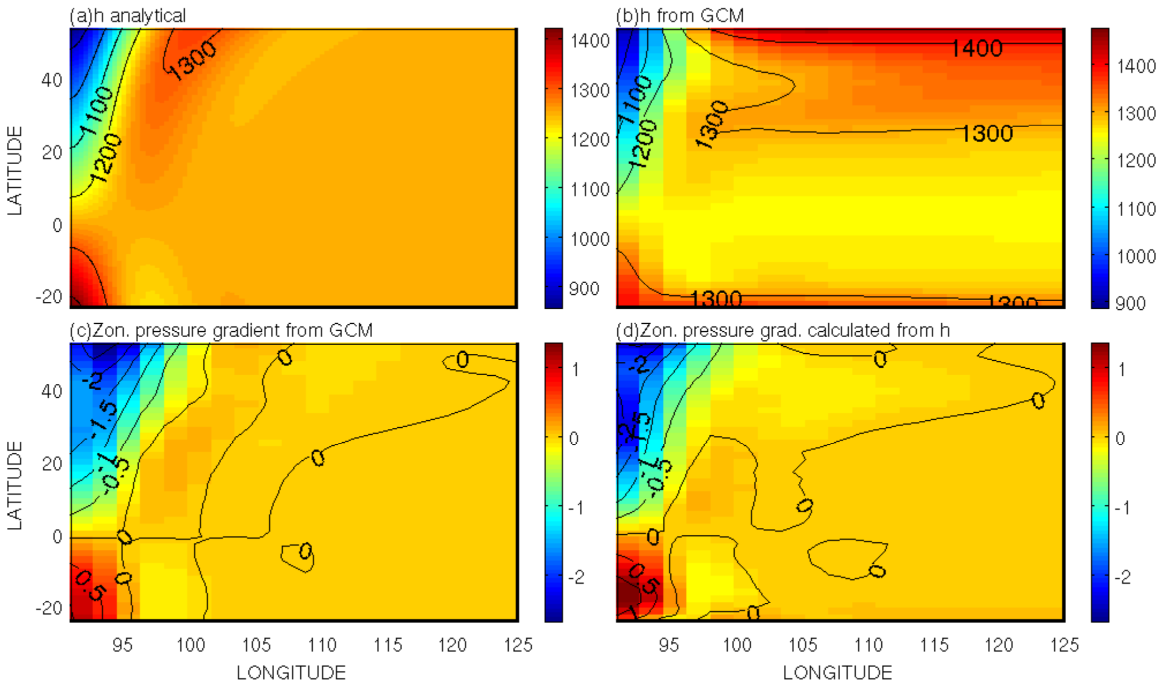

Figure 8: a) Depth of AAIW-NADW interface h (m) calculated from Eq. 3, b) Depth of AAIW-NADW interface h (m) obtained from annual average GCM output, c) zonal pressure gradient (Pa/m) obtained from annual average GCM output and d) zonal pressure gradient (Pa/m) obtained from the zonal slope of the interface h (h obtained from GCM). Note that the western boundary of the idealized Atlantic is at 90 °Longitude.

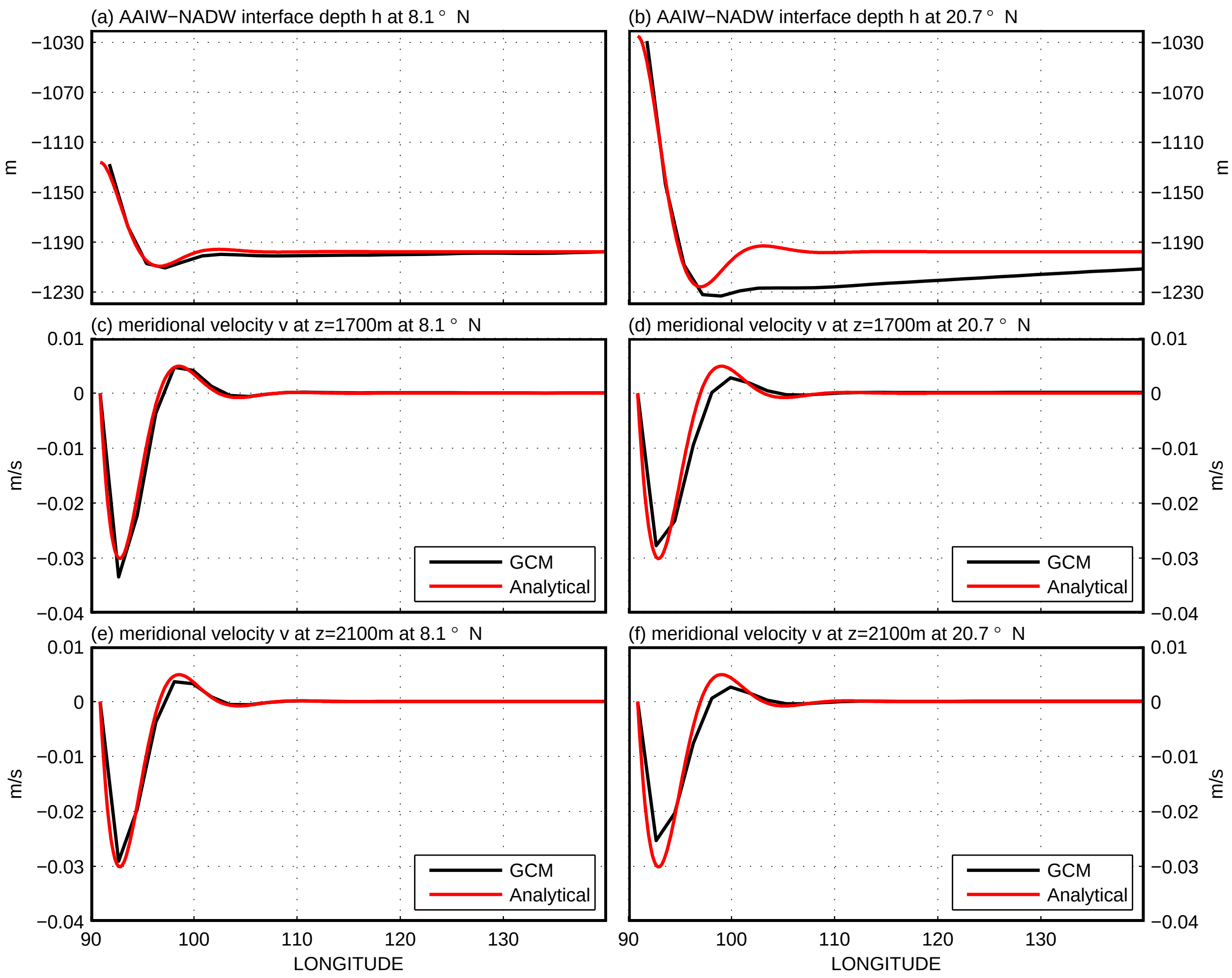

Figure 9: Longitudinal section at the western Atlantic boundary at 8.1 °N (left column) and 20.7 °N (right column) of a,b) the depth of AAIW-NADW interface h (m), c,d) the meridional velocity v (m/s) at 1700m depth and e,f) the meridional velocity v (m/s) at 2100m depth. The values obtained from the numerical model are shown in black, and the analytical values are in red. We choose the average depth $\bar{h}$ at the western boundary at the equator, and the slope s_y as the average slope between 10 degrees North and South. Note that the western boundary of the idealized Atlantic is at 90 °Longitude.

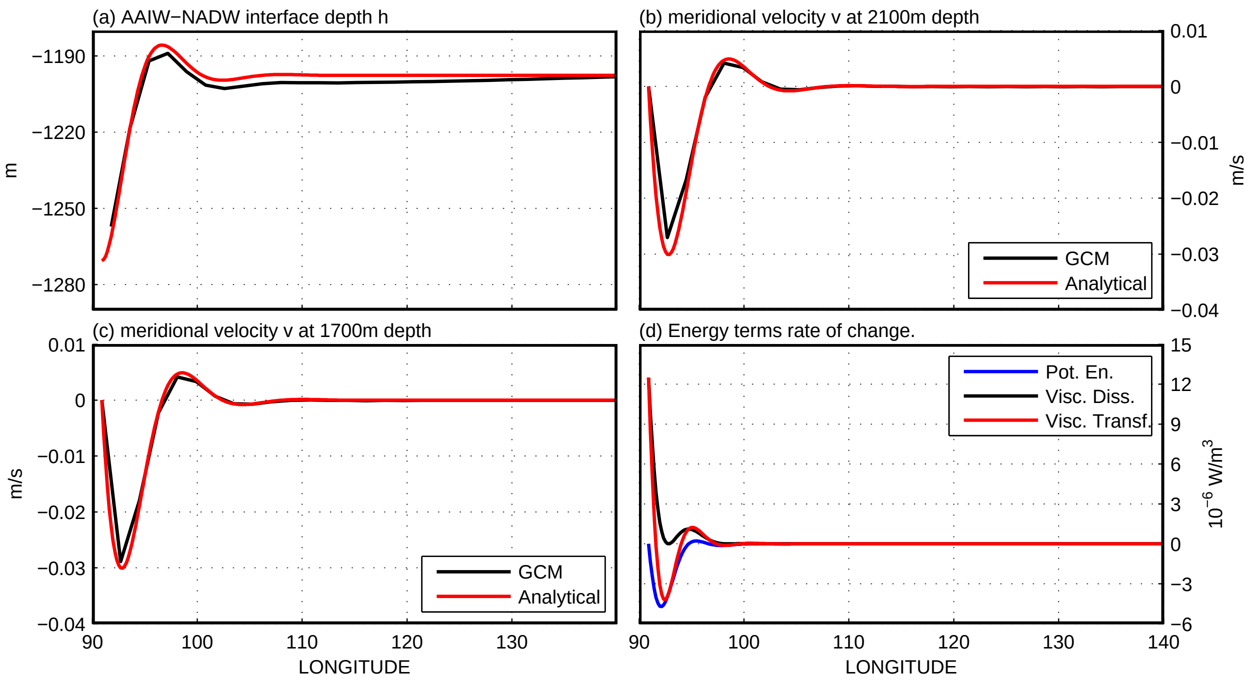

Figure 10: Longitudinal section at the western Atlantic boundary at 8.1 °S (not to be confused with previous Figure showing 8.1 °N) of a) the depth of AAIW-NADW interface h (m), b) the meridional velocity v (m/s) at 2100m depth, c) the meridional velocity v (m/s) at 1700m depth and d) the rate of energy conversion terms ($10^{-6}W/m^3$): potential energy (blue), viscous dissipation (black) and viscous transfer (red). The values obtained from the numerical model in (a), (b) and (c) are shown in black, and the analytical values are in red. $\bar{h}$ and s_y are chosen as in the previous figure.

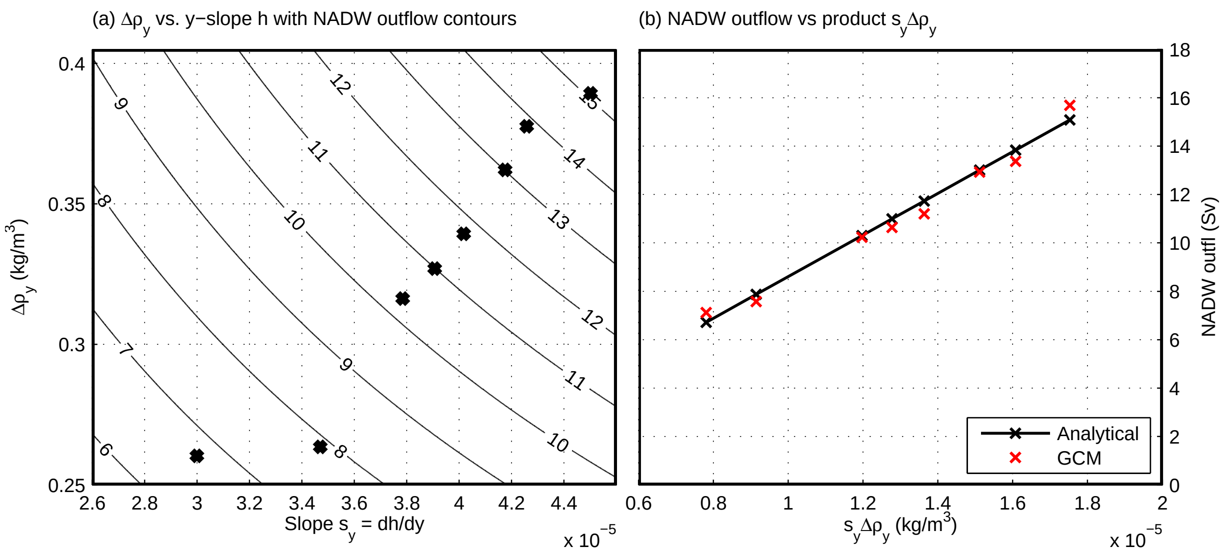

Figure 11: Experiments where atmospheric moisture diffusivity is varied to accomplish oceanic surface buoyancy flux changes. a) NADW outflow rate M (Sv) as a function of the meridional slope $s_y = \frac{\partial h}{\partial y}$ of h and the AAIW-NADW density difference $\Delta\rho$ (kg/m^3). Numerical experiment values are marked by a *. b) NADW outflow rate M (Sv) vs. the product $s_y \Delta\rho$ (kg/m^3) for the numerical model (red) and analytical model (black).